Energy Storage Materials 45 (2022) 1109–1119

Contents lists available at ScienceDirect

Energy Storage Materials

journal homepage: www.elsevier.com/locate/ensm

# Li migration, nucleation and growth behavior regulated by a lithiophilic cobalt phosphide-doped carbon nanofibers derived ion/electron conductive framework

Cuimei Fu[a], Shiru Lin[b], Chengcheng Zhao[a], Jin Wang[a], Lina Wang[a,**], Junwei Lucas Bao[b,*], Yonggang Wang[c], Tianxi Liu[a,d,**]

[a] State Key Laboratory for Modification of Chemical Fibers and Polymer Materials, College of Materials Science and Engineering, Donghua University, Shanghai 201620, China
[b] Department of Chemistry, Boston College, Chestnut Hill, MA 02467, USA
[c] Department of Chemistry, Fudan University, Shanghai 200433, China
[d] Key Laboratory of Synthetic and Biological Colloids, Ministry of Education, School of Chemical and Material Engineering, Jiangnan University, Wuxi 214122, China

ARTICLE INFO

*Keywords:*
Li deposition behavior
Li-metal anode
CoP
Nanofibers
*In-situ* characterizations

ABSTRACT

The uncontrollable Li dendritic plating and infinite volumetric expansion significantly plague the practical applications of lithium (Li) metal, which is regarded as the most promising high-energy-density anode material for rechargeable batteries. The well regulated Li-ion ($Li^+$) flux distribution and Li deposition is the prerequisite for feasible Li-metal batteries. In this work, the Li migration, nucleation and growth behavior are investigated with a lithiophilic CoP-doped carbon nanofibers (CoP@CNF)-guided self-standing substrate. The high adsorption effect and low migration barrier of CoP to $Li^+$ lead to the reversible conversion reaction between Li and CoP, enabling an even charge transportation and a homogeneous $Li^+$ concentration gradient. The uniform nucleation and dense electrodeposition of Li over through the CoP@CNF is demonstrated via combined *in-situ/ex-situ* morphologic and electrochemical characterizations. Benefiting from the small nucleation and growth overpotential of Li, the symmetrical cell of CoP@CNF@Li can steadily operate under 0.5 mA $cm^{-2}$ over 2000 h with a low voltage hysteresis of ca. 12 mV. When paired with a $LiFePO_4$ cathode, a specific capacity exceeding 90 mAh $g^{-1}$ up to 1000 cycles is achieved at 5 C (1 C = 170 mA $g^{-1}$), demonstrating the dendritic Li suppression capability of the CoP@CNF@Li composite anode.

## 1. Introduction

The demand for long-mileage electric vehicles and high-energy-density storage devices has boosted the development of upgraded lithium (Li)-ion chemistry [1–3]. Li-metal batteries with a Li-metal anode which possesses the lightest density (0.534 g $cm^{-3}$), the lowest electrochemical potential (−3.04 V vs. the standard hydrogen electrode) and an ultrahigh theoretical capacity (3860 mAh $g^{-1}$), have attracted extensive research attention [4,5]. Nevertheless, serious challenges regarding cyclability and safety have substantially impeded the practical utilization of Li metal, due to nonuniform electrodeposition behavior embodied as dendritic Li growth and the infinite volume expansion of "hostless" Li [6,7]. The uncontrollable Li dendrites destroy the solid electrolyte interphase (SEI) and expose fresh Li underneath, further accentuating side-reactions with the electrolyte and the branch-like dendrite growth [4,8]. Fractured Li dendrites cause irreversible Li inventory loss, poor Coulombic efficiency (CE) and a short battery lifespan [4,6]. More seriously, these Li dendrites will continue to grow and even fatally penetrate the separator, giving rise to internal short-circuits and safety hazards [3,6,9]. Therefore, the key to suppress dendritic Li growth is tailoring the Li electrodeposition behavior.

Surface pretreatment of Li metal is a plausible approach to inhibit dendritic Li growth. Some endeavors focused on constructing an artificial SEI layer (eg. ion-conductive $Li_3N$ [9–11], LiF [12] or Li-rich alloy layer [13–16], etc.) to accommodate the dendrite formation, while others chose suitable electrolyte additives for building an *in-situ* SEI layer (eg. ionic liquids [17,18], fluoroethylene carbonate [19,20], $LiNO_3$ [21–24], etc.). Nonetheless, the fragile SEI layers can hardly

* Corresponding author.
** Corresponding authors at: State Key Laboratory for Modification of Chemical Fibers and Polymer Materials, College of Materials Science and Engineering, Donghua University, Shanghai 201620, China
*E-mail addresses:* linawang@dhu.edu.cn (L. Wang), lucas.bao@bc.edu (J.L. Bao), txliu@dhu.edu.cn (T. Liu).

https://doi.org/10.1016/j.ensm.2021.11.009
Received 24 July 2021; Received in revised form 15 October 2021; Accepted 2 November 2021
Available online 12 November 2021

withstand the mechanical deformation induced by the infinite volumetric expansion of Li metal during repeated cycles [25]. An alternative approach is to store Li into 3-dimensional (3D) hosts like porous carbon or metal foam (Cu, Ni, etc.) to regulate the Li deposition behavior and buffer the volumetric expansion [26–28]. However, there are risks of Li to be plated outside these electron-conductive scaffolds, particularly at high rates and high deposition capacities. To guarantee that the Li deposits into the 3D structured frameworks, it is necessary to introduce lithiophilic nucleation seeds to guide the Li plating process [29]. An ion/electron-conductive skeleton integrates the advantages of both ion- and electron conducting pathway into a mixed scaffold [30]. The charge diffusion and distribution are facilitated to inhibit the dendritic Li formation due to their unique geometry and lithiophilic chemical constituents [25–37]. For example, Zhang et al. built a scaffold that incorporates $Li_{6.4}La_3Zr_2Al_{0.2}O_{12}$ nanoparticles [31]. Zhai et al. constructed $Cu_2S$ nanowires coated porous Cu foam, the generation of a $Li_2S$ layer has balanced the transport rate of $Li^+$ ions and electrons [33]. Shi et al. assembled a $Ti_3C_2T_X$ MXene-melamine foam with electronic and ionic transport channels [35]. And Zhang et al. introduced $Li_3N$ and LiAl alloy into a mixed ion/electron composite structure [36]. Stable Li plating/stripping at enhanced current densities highlighted the suitability of the mixed conductive skeletons for Li-metal batteries. In spite of this significant progress, there is insufficient understanding of the Li deposition kinetics and the underlying reaction mechanism. Moreover, a readily obtained lithiophilic mixed ion/electron-conducting skeleton with effective Li storage is still in an urgent need.

In this study, a lithiophilic CoP-doped carbon nanofibers (CoP@CNF)-guided dendrite-free Li-metal anode with extend cyclic life is proposed by tailoring the migration of $Li^+$ ions and the subsequent nucleation and growth behavior of Li. The high adsorption energy and fast diffusion rate of $Li^+$ on the lithiophilic CoP, verified from density functional theory (DFT) calculations, lead to abundant nucleation sites for Li. The reversible conversion reaction between Li and CoP guarantees a homogeneous $Li^+$ flux distribution. Uniform nucleation and dense deposition of Li are elucidated via combined *in-situ/ex-situ* morphologic observations and electrochemical characterizations. The symmetric cells of the CoP@CNF@Li anode exhibit a long lifespan up to 2000 (500 cycles), 1000 (500 cycles) and 100 h (250 cycles) under current densities of 0.5, 1 and 5 mA $cm^{-2}$, respectively. An average CE of 98.8% for 400 cycles at 1 mA $cm^{-2}$ and 97.1% at 5 mA $cm^{-2}$ with a capacity of 1 mA h $cm^{-2}$ is maintained. The stable cycling of the cell with a $LiFePO_4$ cathode at high current densities further demonstrates the prospect of the electron/ion conductive CoP@CNF skeleton.

## 2. Experimental methods

### 2.1. Synthesis of CoP@CNF

The precursor nanofibers of CoP@CNF were prepared by an electrospinning method at room temperature. Briefly, 0.38 g cobaltous acetate tetrahydrate ($C_4H_6CoO_4 \bullet 4H_2O$, 99.5%, Sinopharm Chemical) and 0.16 g phosphorus oxide ($P_2O_5$, 98%, Sinopharm Chemical) were dissolved in 10 mL of *N,N*-dimethylformamide (DMF, $C_3H_7NO$, 99.5%, Sinopharm Chemical) to get a homogeneous solution after sonication for 20 mins. Then, 1 g polyacrylonitrile (PAN, average Mw 150,000, Sigma-Aldrich) was dissolved in the solution under vigorous stirring for 12 h. Subsequently, the as-obtained solution was loaded into a syringe to electrospin by applying a work voltage of 15–20 kV (ET2531, Beijing Ucalery Technology). Finally, the as-obtained nanofibers were calcined in a tubular furnace at 800 °C for 2 h under nitrogen atmosphere with a heating rate of 5 °C $min^{-1}$. As a control, a CoP-free CNF was synthesized at the similar conditions without addition of $C_4H_6CoO_4 \bullet 4H_2O$ and $P_2O_5$ in the precursor solution. The mass loading of the obtained CoP@CNF and CNF was controlled to be ca. 3.0 mg $cm^{-2}$.

### 2.2. Material characterization

The microstructure of CoP@CNF was investigated by scanning electron microscope (SEM, 7500F, JEOL) and transmission electron microscope (TEM, Talos F200S, FEI) with high-angle annular dark-field detector (HAADF-STEM) and X-ray energy dispersive spectroscope (XEDS) elemental mapping analysis. Powder X-ray diffractometer (XRD) patterns were performed on an X-ray diffractometer (D/max-2500VB+/PC, Rigalcu) equipped with Cu K$\alpha$ radiation. The samples were covered by a piece of polyethylene (PE) film to prevent the atmospheric contamination during the XRD measurement. The chemical valence was identified by X-ray photoelectron spectroscopy (XPS, Escalab 250Xi, Thermo Fisher Scientific). The weight (wt%) of CoP in the CoP@CNF was measured by thermogravimetric analysis (TGA), which was conducted on a TG analyzer (NETZSCH TG 209 F1 Libra) in the temperature ranging from ambient to 900 °C under air atmosphere. The relative content (wt%) of carbon and nitrogen was confirmed by elemental analysis (VarioEL III). Raman spectroscopy (inVia-Reflex, Renishaw) was carried out to analyze the coordination structures of CoP@CNF. The nitrogen sorption/desorption measurements were conducted on a Quadrasorb adsorption instrument (Quantachrome Instruments). The specific surface area was calculated according to the multipoint Brunauer–Emmett–Teller (BET) method.

### 2.3. Electrochemical performance

Battery performance was evaluated with CR2025 coin-type cells on a Land CT2001A instrument (Wuhan, China) at room temperature. The polypropylene/polyethylene microporous membrane (celgard 2325, 16 mm in diameter, 25 $\mu$m thick) was supplied as the separator. 1.0 M lithium bis(trifluoromethanesulfonyl) imide (LiTFSI) in 1,3-dioxolane (DOL)/1,2-dimethoxyethane (DME) (1:1, vt%) in presence of 0.2 M $LiNO_3$ was employed as the electrolyte. To investigate the electrochemical deposition of Li, coin cells assembled with Li metal foil ($d$ = 14 mm) as counter/reference electrode. To estimate the Li plating/stripping behavior of CoP@CNF@Li, symmetric cells with two pieces of identical electrodes was assembled. Cyclic voltammetry (CV) at the scanning rate of 0.1 mV $s^{-1}$ in a voltage window of −0.2–0.2 V (vs. $Li/Li^+$) was carried out on CHI660E electrochemical workstation. Electrochemical impedance spectroscopy (EIS) measurements were performed under an opencircuit potential with an amplitude of 0.05 mV in the frequency range of 0.01–100 kHz. The CoP@CNF@Li electrodes were washed thoroughly with DME to remove the lithium salt before SEM and XRD measurements. The electrochemical measurements of controlled CNF and Li foil samples were conducted under the same conditions.

$LiFePO_4$ was employed as the cathode to evaluate the feasibility of the CoP@CNF@Li anode. The cathode was prepared by casting a mixture slurry of 90 wt% $LiFePO_4$, 5 wt% super P carbon additive and 5wt% PVdF binder in N-methyl-2-pyrrolidone ($C_5H_9NO$, 99.0%, Shanghai Lingfeng Chemical) on aluminum foil. After drying, the cathodes were punched into discs ($d$ = 12 mm) with a mass loading of 10 mg $cm^{-2}$ (1.5 mAh $cm^{-2}$) afterwards to couple with CoP@CNF@Li anodes ($d$ = 12 mm, 10 mAh $cm^{-2}$). The potential window was configured within 2–4 V (vs $Li/Li^+$). As a control, CNF@Li and Li foil were implemented for the measurements in the same configuration. The pre-electrodeposited Li on CNF@Li and CoP@CNF@Li is 10 mAh $cm^{-2}$ for symmetrical cells or that to be coupled with $LiFePO_4$.

### 2.4. Computational method

We performed plane-wave spin-polarized density-functional theory (PW-DFT) computations by *Vienna ab initio simulation package* (VASP, version 5.3) [38], with the projector-augmented-wave (PAW) method [39]. We used the Perdew-Burke-Ernzerhof (PBE) density functional [40], and Grimme's D3 dispersion correction with the Becke-Johnson

(BJ) damping function [41–44]. To explore the most stable surface of CoP and $Li_3P$, we carved out the (111), (110), (100) facets from the optimized bulk structures. The unit cell contains 32 Co and 32 P atoms in the slab models for the (110) and (100) facets, and 64 Co and 64 P atoms for the (111) facet of CoP. There are six layers in the (111) facet of CoP, and the bottom three layers are fixed in the geometry optimization. For all three facets of the $Li_3P$ slab models, the unit cell contains four layers, 96 Li and 32 P atoms, and the bottom two layers are fixed. The Monkhost-Pack-sampled 3 × 3 × 1 *k*-points meshes with a first-order Methfessel-Paxton smearing parameter of 0.1 eV were used in all calculations [45]. The kinetic-energy cutoff of the plane-wave basis was set to 380 eV. The forces were converged within 0.023 eV/Å for the optimization of local minima, and 0.05 eV/Å for the transition-state structures, which were determined by the climbing image nudged elastic band (CI-NEB) method [46]. A vacuum layer of 15 Å normal to the surface was added between the slabs so that there is no artificial interaction between the image slabs, along with a dipole correction [47]. The lithium adsorption energies were computed by the following Eq. (1):

$$E_{ad} = E_{(Li+s)} - E_s - E_{Li} \quad (1)$$

where $E_{(Li+s)}$ is the electronic-structure energy of Li atom adsorbing on the slab, $E_s$ is the electronic-structure energy of clean slab, and $E_{Li}$ is for a single isolated Li atom (the energy of which is computed in a large asymmetric cell).

We computed the real-space charge density differences by the following Eq. (2) and visualized them by using VESTA [48]

$$\Delta\rho = \rho_{(Li+s)} - \rho_s - \rho_{Li} \quad (2)$$

where $\rho_{(Li+s)}$ is the charge density of Li adsorbing on the slab; $\rho_s$ is the charge density obtained from a single-point calculation based on the slab geometry directly carved out from the Li+s system; the slab is isolated but not re-optimized; $\rho_{Li}$ is the charge density of a single isolated Li atom. The yellow region represents partial electron gain (i.e., $\Delta\rho > 0$), whereas the blue region represents the loss of electrons (i.e., $\Delta\rho < 0$). $\Delta\rho$ characterizes the direction of the charge transfer during the adsorption process.

We computed the Gibbs free energy change ($\Delta G$) of reaction CoP + 3Li = Co + $Li_3P$ at the discharging voltage (0.1 V) and the reverse reaction Co + $Li_3P$ = CoP + 3Li at the charging voltage (3.0 V) by the following Eq. (3):

$$\Delta G = \Delta E + \Delta ZPE - T\Delta S + \Delta G(U) \quad (3)$$

where $\Delta E$ is the reaction energy obtained from the DFT self-consistent field (SCF) energies and $T$ is the temperature in Kelvin. $\Delta ZPE$ and $\Delta S$ are the change of vibrational zero-point energy and the reaction entropy. $\Delta G(U)$ is the free energy contribution related to applied voltage $U$, which can be determined as the following Eq. (4):

$$\Delta G(U) = -zFU \quad (4)$$

where $z$ is the number of the charge transferred during the reaction (in mole), $F$ is Faraday constant (96,484.5 C $mol^{-1}$). For the isolated Co and Li atoms, the $S$ values were taken from the NIST database [49]. The $S$ values for gas-phase Li atoms are 0 and 0.0014 eV $K^{-1}$ under 0 K and 298.15 K. And those for gas-phase Co atoms are 0 and 0.0019 eV $K^{-1}$ under 0 K and 298.15 K, respectively. For CoP and $Li_3P$, the ZPE and $S$ values were obtained from vibrational frequency computations under the harmonic-oscillator approximation and were averaged by the number of repetitive structural motifs in each computational unit cell. The unit cells for the frequency computations of the bulk CoP and $Li_3P$ contain 4 Co and 4 P, and 6 Li and 2 P atoms, respectively. We used 7 × 10 × 6 and 9 × 9 × 4 Monkhost-Pack *k*-points for CoP and $Li_3P$, respectively. The SCF convergence threshold was set to $10^{-5}$ eV. We used the Shermo module implemented in VASPKIT [50] to compute the values of ZPE by summing over all normal modes and $S$ by using the harmonic-oscillator vibrational partition functions.

## 3. Results and discussion

### 3.1. Synthesis and material characterizations of CoP@CNF

The synthesis of CoP@CNF composite is realized by a facile electrospinning method and a subsequent *in-situ* carbothermic reduction process. In brief, the electrospun films were prepared from a DMF solution with PAN, $C_4H_6CoO_4 \bullet 4H_2O$, and $P_2O_5$. Wherein, PAN provided the desirable rheological property and carbon source. The precursor film was then thermally treated under $N_2$ atmosphere at 800 °C for 2 h to acquire CoP@CNF via a carbothermic reduction reaction. During the pyrolysis process, a strong reducing atmosphere (eg. carbon, CO and $H_2$) was released (Fig. S1), and the high valence phosphate was *in-situ* reduced to form CoP in the CNF. As schematically illustrated in Fig. 1a, compared with the undoped CNF, the lithiophilic CoP@CNF derived ion/electron skeleton holds the promise toward a dendrite-free Li-metal anode by regulating the $Li^+$ flux distribution at a fast rate.

The as-prepared CoP@CNF film is robust and flexible (Inset in Fig. 1b). SEM images show the network of interconnected nanofibers with a uniform diameter ca. 500 nm (Fig. 1b), and a wrinkled surface ascribed to the pyrolysis process is observed (Fig. 1c). High-resolution TEM images reveal that the CoP nanoparticles with clearly identified lattice fringes (112) are uniformly distributed throughout the nanofibers (Fig. 1d). The XEDS of CoP@CNF shows the homogeneous distribution of Co, P, N, and C elements in nanofibers (Fig. 1e). The C and N atoms are originated from pyrolytic PAN. Analogous features are observed from CNF without CoP incorporation (Fig. S2). The BET surface areas of the CoP@CNF and CNF were calculated to be 75.2 and 19.4 $m^2\ g^{-1}$, and the total pore volumes were 0.10 and 0.02 $cm^3\ g^{-1}$, according to the $N_2$ adsorption-desorption isotherms (Fig. S3a). The porous structure of hierarchical mesopores and macropores was formed due to the gas activation and internal crystallization of CoP during the carbonization process in the CoP@CNF host (Fig. S3b).

The crystalline structures of the as-prepared CoP@CNF and CNF were investigated by XRD (Fig. 1f). It should be noted that a 50% excess of $P_2O_5$ was required for pure-phase CoP to compensate for its volatilization during calcination at 800 °C. The diffraction patterns of the CoP@CNF exhibit several peaks corresponding to orthorhombic CoP (JCPDS no. 29–0497). The broad diffraction peak situated at 26° corresponds to the graphitic (003) plane (JCPDS no. 26–1077). The Raman spectra of both CoP@CNF and CNF show characteristic of D (1345 $cm^{-1}$, diamondlike) and G bands (1580 $cm^{-1}$, graphitelike) (Fig. S4). The intensity ratios ($I_D/I_G$) of CoP@CNF and CNF are 1.056 and 1.019, respectively, indicating a relatively high defect density in CoP@CNF. TGA was implemented to verify the content of CoP in the CoP@CNF (Fig. S5), which was calculated to be ca. 41 wt%. Elemental analysis (Table S1) confirms the respective C content is 43 and 81 wt% in CoP@CNF and CNF, and the N content is 6 and 14 wt%.

XPS measurements were conducted to probe the chemical composition and elemental valence of the CoP@CNF, which further confirms the presence of Co, P, N, C and O elements (Fig. S6a). The Co 2p spectrum shows a pair of apparent peaks at 778.7 eV and 793.6 eV, corresponding to Co $2p_{3/2}$ and Co $2p_{1/2}$ of CoP [51,52], respectively (Fig. 1g). In addition, the doublet at 780.9 and 797.7 eV can be ascribed to the surface oxidized Co species during the thermal treatment [52], and a split blip of shakeup satellite (sat.) peaks of Co 2p spectra situate at 784.6 and 802.8 eV [53]. The peaks fitted at 130.9 and 129.8 eV in the P 2p spectrum can be assigned to P $2p_{1/2}$ and $2p_{3/2}$ of CoP [51], respectively (Fig. 1h). The P species at 132.6 and 133.9 eV are ascribed to the C-P bond and superficial oxidation state of the P bonded to O atoms [54]. The signals ascribed to graphitic N (401.1 eV), pyrrolic N (399.7 eV) and pyridinic N (398.4 eV) are detected in the N 1 s spectrum (Fig. S6b) [55–57]. The C 1 s spectrum is deconvoluted into three components situated at 287.4, 285.5 and 284.6 eV, which respectively correspond to O–C = O, C–N/C-P and graphitic C atoms (Fig. S6c) [58].

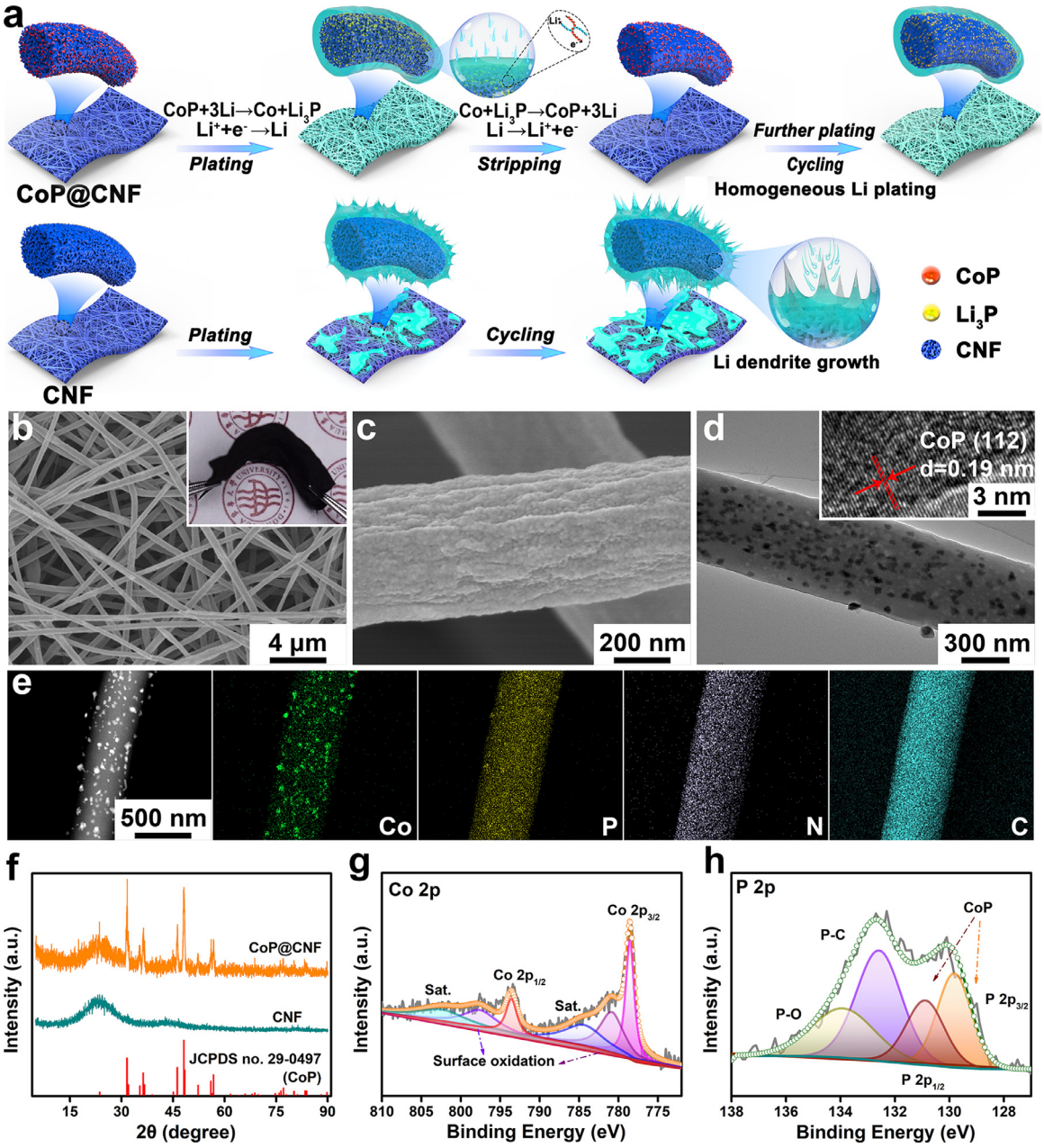


**Fig. 1.** (a) Schematic illustration of Li plating/stripping on CoP@CNF and CNF. (b) SEM image of the self-standing CoP@CNF film. The inset white box is a digital picture. (c) SEM and (d) TEM images of a single CoP@CNF nanofiber. The inset is high-resolution TEM image of CoP (112). (e) The corresponding elemental mapping of Co, P, N and C. (f) XRD pattern and high-resolution XPS spectra of (g) Co 2p and (h) P 2p for CoP@CNF.

### 3.2. Li plating/stripping behavior of CoP@CNF

The dendrite-inhibiting behavior of CoP@CNF was firstly evaluated by operando optical microscope observation. Three electrochemical cells were assembled with Li, CNF or CoP@CNF as the working electrode, and the counter electrode is Li foil. Mossy Li dendrites are generated quickly on Li metal surface even at the initial stages (Fig. 2a). Uneven dendritic Li is visible after 30 min on CNF film due to the inhomogeneous $Li^+$ gradient distribution (Fig. 2b), and the loose Li protuberances continue growing in the following plating process. Upon Li plating, severe volumetric expansion was clearly observed in terms of the Li and CNF electrodes. In contrast, a smooth surface without observable dendrites is observed on CoP@CNF throughout the entire process (Fig. 2c).

To probe the origin of the lithiophilicity and nucleation behavior of CoP@CNF to Li, the initial adsorption energy was investigated on the basis of DFT calculations (Fig. 2d). The optimized structures of CoP, graphene and N-doped graphene (graphitic N graphene as representative, donated as "GrN graphene") were constructed (Fig. S7a–c). CoP (100) is the most stable surface for CoP, which has energies 0.42 and 0.24 eV (per pair of Co and P) lower than the surface (111) and (110) after full relaxation (Fig. S7d–f). CoP (100) surface has two stable adsorption sites for Li, named as Co site and P site (Fig. S8). Compared with graphene (−0.77 eV) and GrN graphene (−0.78 eV), the adsorption energy of the most favorable Co site of CoP (100) (−3.33 eV) is much more negative (Fig. 2e). A large adsorption energy indicates the Li adsorption on CoP is much easier than on graphene and GrN graphene, leading to a lower Li nucleation barrier [59]. Therefore, the distribution of

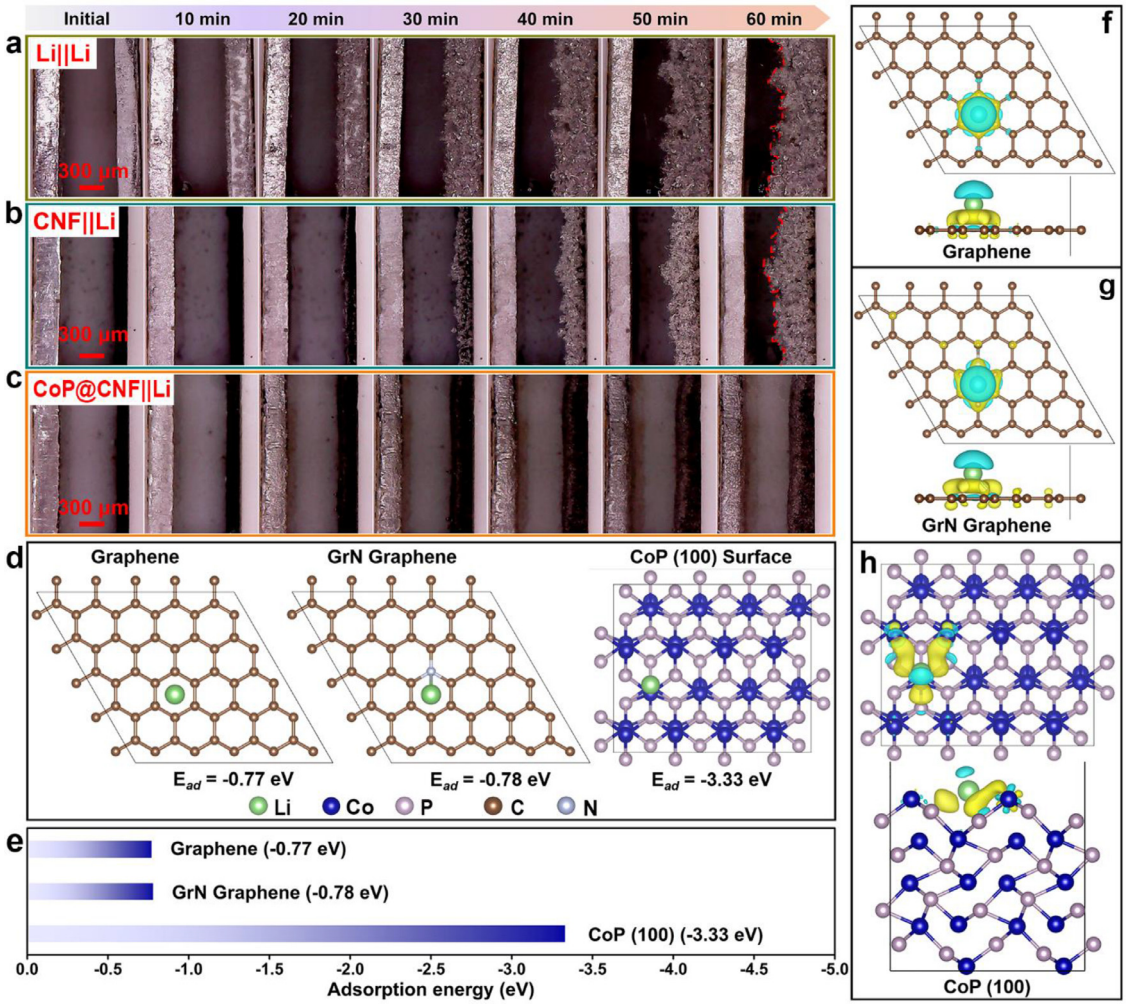


**Fig. 2.** The *operando* optical microscopy of Li plating behavior on (a) Li foil, (b) CNF and (c) CoP@CNF. The left side is Li metal counter electrode. (d) DFT (PBE-D3BJ) adsorption geometries and energies ($E_{ad}$, in eV) of Li atom on graphene, GrN graphene and CoP (100) surface. (e) A comparison of the computed adsorption energies. The top and side views of the real-space charge density differences for the adsorption of Li on (f) graphene, (g) GrN graphene and (h) CoP (100). The blue color represents a decrease in the charge density after adsorption, and the yellow color represents an increase. The charge density differences are plotted with an isosurface value of 0.0025*e*.

CoP on carbon nanofiber should have an enhanced adsorption capacity for Li.

The electronic charge difference before and after the adsorption of Li on CoP, graphene, and GrN graphene leads to a better understanding of their interaction mechanisms with Li. For graphene (Fig. 2f), Li transfers electrons to six neighboring carbon atoms, and the carbon atoms next to these neighboring carbon atoms lose some electrons to form a bond between Li and graphene, reducing the strength of $\pi$ bonding and the stability of graphene. GrN graphene has a similar interaction mechanism to graphene, but it obtains more electrons from the Li atom (Fig. 2g). The interaction mechanism of CoP departs from graphene, as the Li atom interacts not only with the centered Co in CoP (110), but also with the nearby two Co and two P atoms (Fig. 2h). Contributed by the unpaired electrons from Co *d* orbitals and P *p* orbitals, a strong bonding strength of Li on CoP surface was attained. These results indicate that CoP@CNF can provide sufficient nucleation sites for uniform Li deposition, which is in well accordance with its adsorption energy.

To evaluate the lithiophilicity, the Li nucleation overpotential ($\mu_n$) on CoP@CNF or CNF was investigated with Li foil as the counter electrode. Fig. 3a shows the voltage profiles of Li plating at 0.5 mA cm$^{-2}$ for 10 mAh cm$^{-2}$ (20 h). Two plateaus are observed at ca. 1.7 and 0.9 V for the CNF electrode, which is ascribed to the reaction of Li with C = N bonds in the framework to form Li–C–N–Li [60] and the adsorption of $Li^+$ into the porous structure of nanofibers [61,62], respectively. The slope below 0.5 V corresponds to the insertion of $Li^+$ into graphitic carbon layers. The last plateau at ca. 0 V is attributed to the plating of Li at nucleation sites. In terms of CoP@CNF, the conversion reaction between CoP and Li (CoP + 3Li ↔ $Li_3P$ + Co) would occur during the Li nucleation process. The general sloping voltage profile indicates a pseudocapacitive dominated $Li^+$ storage mechanism originating from the nanosized CoP. Pseudocapacitive charge storage through fast surface reactions on CoP allows for high charge/discharge rates [63,64]. Based on the loading of CoP (1.2 mg cm$^{-2}$), the amount of Li for CoP lithiation is 0.3 mg cm$^{-2}$. The full lithiation of CoP needs ca. 2.3 h at the current of 0.5 mA cm$^{-2}$. The prolonged profile within the wide voltage range above 0 V is resulted from the Li interaction with N– doped carbon substrate, because weak plateaus at ca. 1.7 and 0.9 V are also detectable. The larger amount of C/N in CNF should be responsible for the slightly higher charge at the initial period of Li plating. Compared to that of 16 mV for CNF, the Li nucleation overpotential is only 9 mV for CoP@CNF, indicating a better affinity to Li. In the plating process, the growth overpotential of the CoP@CNF (14 mV) is smaller than CNF (24 mV), implying a feasible growth process of the Li crystal nucleus on CoP@CNF. Even at 1 mA cm$^{-2}$, CoP@CNF was able to obtain a $\mu_n$

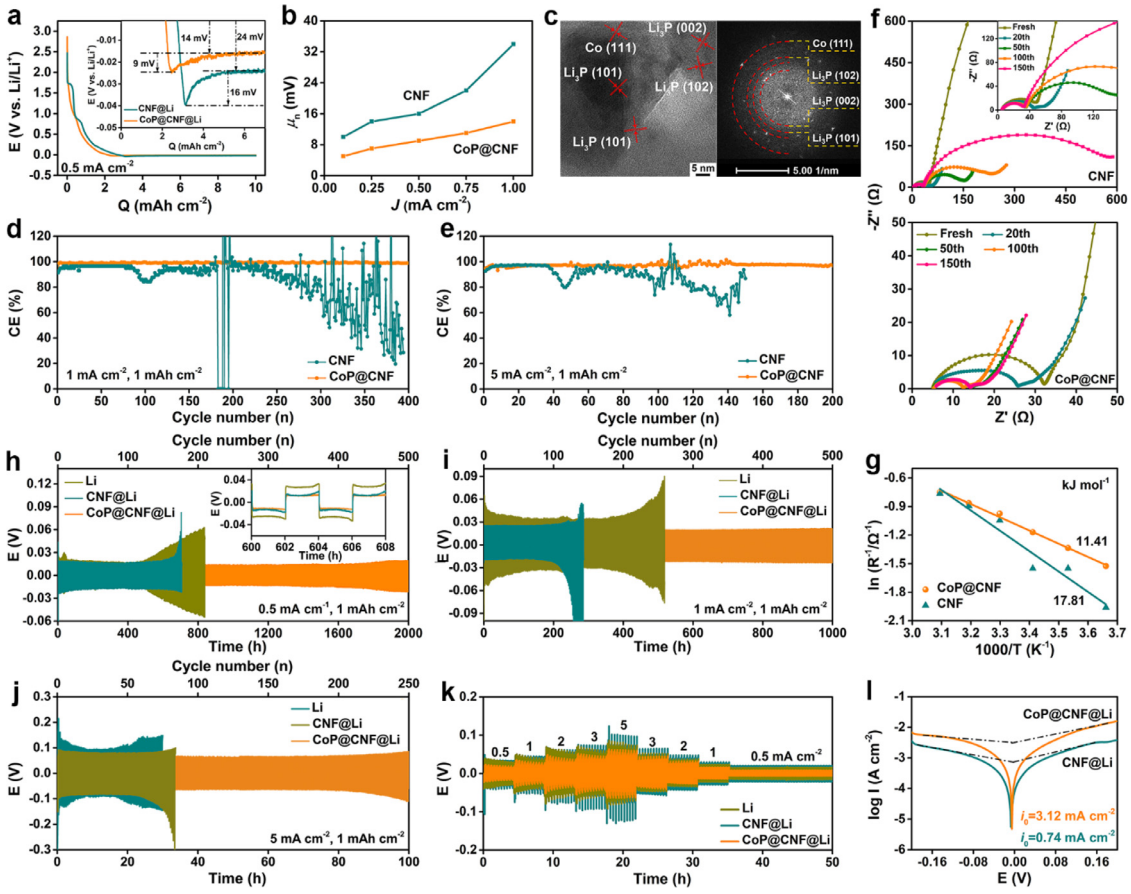


**Fig. 3.** (a) The voltage–capacity curves at 0.5 mA cm$^{-2}$ and (b) nucleation overpotential ($\mu_n$) at different current densities ($J$) of CoP@CNF and CNF. (c) HRTEM image and FFT pattern at 0.1 V of CoP@CNF. Coulombic efficiency at (d) 1 and (e) 5 mA cm$^{-2}$, (f) EIS plots at different cycle states at 1 mA cm$^{-2}$ of CoP@CNF||Li and CNF||Li cells. The inset is the enlarged plots at high frequency. (g) The activation energy for $Li^+$ diffusion. Galvanostatic cycling performance of the symmetric cells with different electrodes at (h) 0.5, (i) 1 and (j) 5 mA cm$^{-2}$. (k) Rate performance of the symmetric cells. (l) Tafel profile obtained from CV measurements. The capacity is limited to 1 mAh cm$^{-2}$.

of 15 mV, which is lower than that of 34 mV for CNF (Fig. 3b). XRD was conducted to validate the electrochemical reaction products after discharge to 0.1 V and stripping to 3 V (Fig. S9). The identification of $Li_3P$ (JCPDS no. 74–1160) at 0.1 V and CoP (JCPDS no. 29–0497) at 3 V further confirms the reversible conversion reaction between CoP and Li. $Li_2CO_3$ impurity was also detected for both samples, which is expected derived from the side reactions of the electrolyte with the active Li. The lattice fringes of $Li_3P$ and Co (JCPDS no. 15–0806) were identified in high-resolution TEM image and corresponding fast Fourier transform (FFT) pattern at 0.1 V (Fig. 3c). The Gibbs free energy change ($\Delta G$) of reaction CoP + 3Li = Co + $Li_3P$ at the discharging voltage (0.1 V) and the reverse reaction Co + $Li_3P$ = CoP + 3Li at the charging voltage (3.0 V) was further computed to validate the reversible reaction. The $\Delta G$ under 298.15 K for CoP + 3Li = Co + $Li_3P$ is −2.63 eV at 0 V and −2.93 eV at 0.1 V (Table S2), which means the forward reaction can occur both spontaneously and under the experimental voltage. Whereas, the $\Delta G$ for the reverse reaction Co + $Li_3P$ = CoP + 3Li under 298.15 K is +2.63 eV at 0 V and −6.37 eV at 3.0 V, indicating that the external electric work compensates for the increase of free energy and thus the stripping process can take place under 3.0 V as well.

The Coulombic efficiency (CE) with a fixed cycling capacity of 1 mAh cm$^{-2}$ followed by stripping to 1.0 V provides further insights of the lithiophilic CoP@CNF. At a moderate current density of 1 mA cm$^{-2}$, the CE of CoP@CNF reaches up to 98.8% over 400 cycles (Fig. 3d). With the current density increasing to 5 mA cm$^{-2}$, a high CE of 97.1% can still be maintained even after 200 cycles (Fig. 3e). In comparison, the CE of CNF deteriorates quickly after 200 cycles at 1 mA cm$^{-2}$ and after 100 cycles at 5 mA cm$^{-2}$. The overpotential of plating/stripping reflects the Li nucleation and growth barrier during cycling. Remarkably, the CoP@CNF exhibits a lower plating/stripping overpotential than CNF at the same current density (Fig. S10), indicating a faster kinetics of $Li^+$ migration in the skeleton. The kinetics of $Li^+$ diffusion and charge transfer are evaluated by electrochemical impedance spectroscopy (EIS) (Fig. 3f). The interfacial transfer resistance ($R_i$) of the CNF||Li undergoes fluctuation. It decreases within 50 cycles and then increases gradually (see the enlarged figure in Fig. 3f), reflecting the establishment and deterioration of the electrode/electrolyte interface. Under 1 mA cm$^{-2}$/1 mAh cm$^{-2}$, the cell before and after 150 cycles is 57 and 578 Ω. In contrast, the CoP@CNF||Li cell shows a much smaller $R_i$ of 32 and 14 Ω, respectively, demonstrating the promoted charge transport at the electrode/electrolyte interface. Furthermore, the temperature-dependent electrochemical impedance spectra were implemented to investigate the activation energy in the range of 273 to 323 K (Fig. S11). The dependent relationship of conductivity on temperature obeys the low of Arrhenius and the corresponding Arrhenius plots are obtained (Fig. 3g) [65,66]. CoP@CNF displays a smaller activation energy (11.41 kJ mol$^{-1}$) than CNF@Li (17.81 kJ mol$^{-1}$), suggesting a faster $Li^+$ transport in the CoP@CNF matrix.

The galvanostatic cyclic performance and the interfacial stability under various current densities were investigated with the symmetrical cells of CoP@CNF@Li and CNF@Li electrodes, which were obtained by predepositing 10 mAh cm$^{-2}$ of Li on CoP@CNF and CNF at 0.5 mA cm$^{-2}$, respectively. A symmetrical Li metal foil cell was also assembled as a control. Impressively, the symmetrical CoP@CNF@Li cell maintains

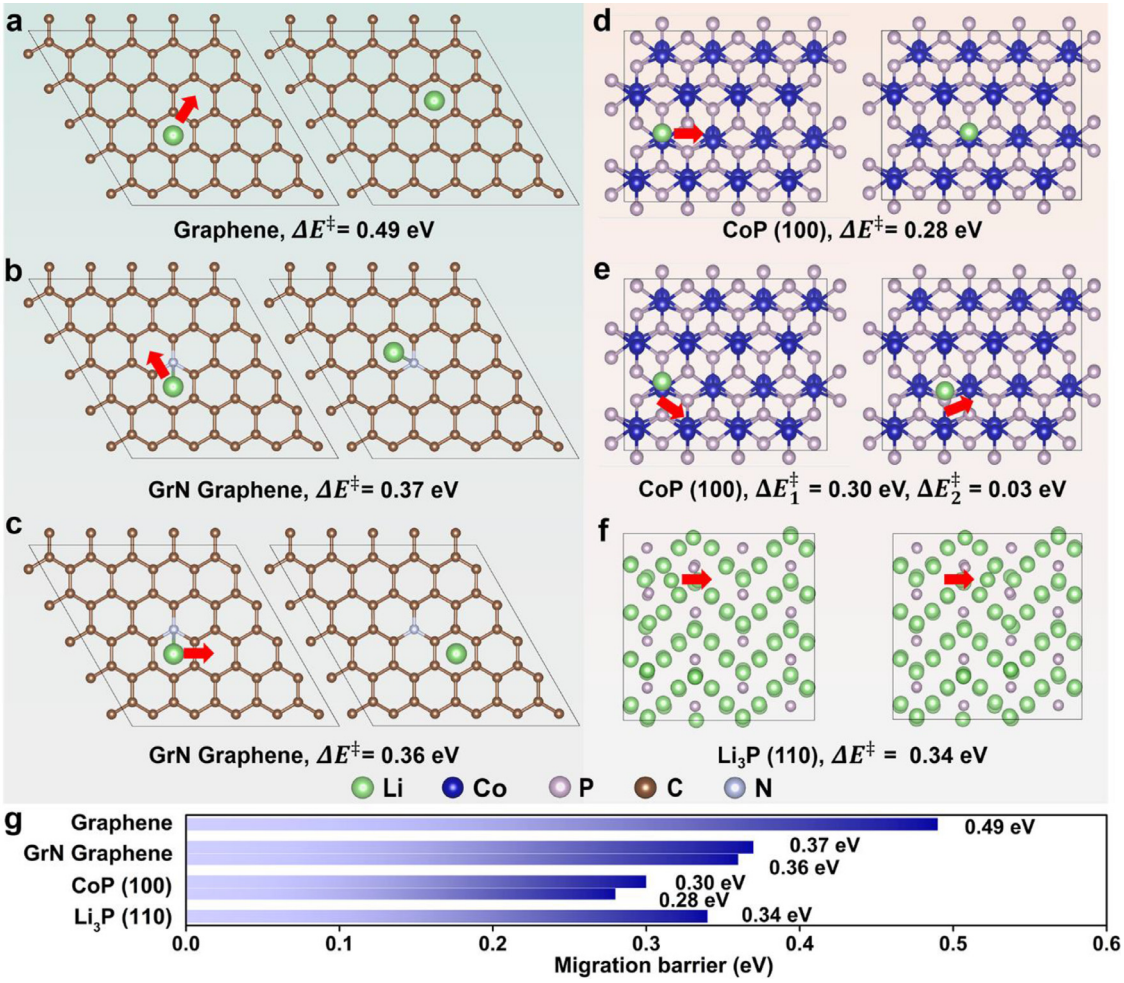


**Fig. 4.** Li migration pathway (indicated by the direction of the red arrow) and the corresponding barrier $\Delta E^{\ddagger}$ (in eV) on (a) graphene, (b and c) GrN graphene, (d and e) CoP (100) and (f) $Li_3P$ (110) surface. (e) The comparison of the Li migration barriers on various materials.

a highly stable voltage profile with a long lifespan over 2000 h (500 cycles, Fig. 3h) and a small voltage overpotential ca. 12 mV at 0.5 mA $cm^{-2}$, 1 mAh $cm^{-2}$. In contrast, the symmetrical CNF@Li exhibits a large overpotential of 19 mV for 700 h (175 cycles) with a sharp overpotential rise to 57 mV. Li foil cells survive for 500 h (125 cycles) with an overpotential of 20 mV following with a severe fluctuation of voltage. At 1 mA $cm^{-2}$, the CoP@CNF@Li shows a stable overpotential of 20 mV for 1000 h (500 cycles), compared with 25 and 34 mV for CNF@Li and Li foil for 250 (125 cycles) and 500 h (250 cycles), respectively (Fig. 3i). Even at 5 mA $cm^{-2}$, CoP@CNF@Li could still obtain stable cycling for 100 h (250 cycles), in contrast with 10 (25 cycles) and 50 h (125 cycles) for CNF@Li and Li foil, respectively (Fig. 3j). Moreover, the CoP@CNF@Li exhibits stable rate capabilities during the switch of different current densities (Fig. 3k). The cycling performance of symmetric cells is among the top results in comparison with the previously reported 3D skeleton Li-metal anode (Table S3). Considering the smaller Li nucleation overpotential of CoP@CNF, the Tafel slopes were determined in accordance with the corresponding cyclic voltammetry plots to further probe the Li redox kinetics at higher overpotentials (Fig. 3l). The CoP@CNF@Li demonstrates an exchange current density ($i_0$) of 3.12 mA $cm^{-2}$, which is higher than that of CNF@Li (0.74 mA $cm^{-2}$), indicating a faster charge-transfer kinetic.

To confirm the $Li^+$ conductivity of CoP and $Li_3P$ (Fig. S12a and b), DFT calculations were conducted to compare $Li^+$ migration barrier energies ($\Delta E^{\ddagger}$) by searching transition states of $Li^+$ diffusions on the stable CoP (100), $Li_3P$ (110) (Fig. S12c–e), graphene, and GrN graphene surfaces. Graphene exhibits a migration barrier for $Li^+$ of 0.49 eV (Fig. 4a). The GrN graphene shows a low migration barrier with 0.37 eV to the neighboring adsorption site near N (Fig. 4b) and 0.36 eV to the next adsorption site surrounded by C atoms (Fig. 4c). Impressively, CoP (100) possesses a fast diffusion rate with an even lower migration barrier of 0.28 eV by direct diffusion (Fig. 4d) and 0.30 eV ($\Delta E_1^{\ddagger}$ = 0.30 eV, $\Delta E_2^{\ddagger}$ = 0.03 eV, Fig. 4e) for indirect diffusion to the next most stable adsorption site. This demonstrates that CoP is quite excellent for modifying electrode materials, not only possessing enhanced adsorption ability but also a low migration barrier for the $Li^+$to obtain homogeneous nucleation sites and $Li^+$ flux. The most stable surface of $Li_3P$ (110) delivers a migration barrier of 0.34 eV (Fig. 4f), which is a favorable transmission path for $Li^+$. Therefore, it can be proved that CoP and $Li_3P$ improve the $Li^+$ migrating rate, which further guarantees homogeneous $Li^+$ distribution and dendrite-free Li deposition (Fig. 4g).

### 3.3. Morphology evolution during cycling

The SEM images at different Li plating–stripping states was investigated to probe the morphological evolution of CoP@CNF. The points of the 1st-plating (I–IV), 1st-stripping (V and VI) and 2nd-plating (VII) were marked in galvanostatic voltage profiles at 0.5 mA $cm^{-2}$ for 10 mAh $cm^{-2}$ (Fig. 5a). Generally, the interconnected 3D nanofibrous network is well maintained upon the continuous Li plating/stripping processes (Fig. 5b). Compared to the pristine nanofibers (Fig. 5b I), a spotted surface is observed at the initial areal capacity of 1 mAh $cm^{-2}$ (Fig. 5b

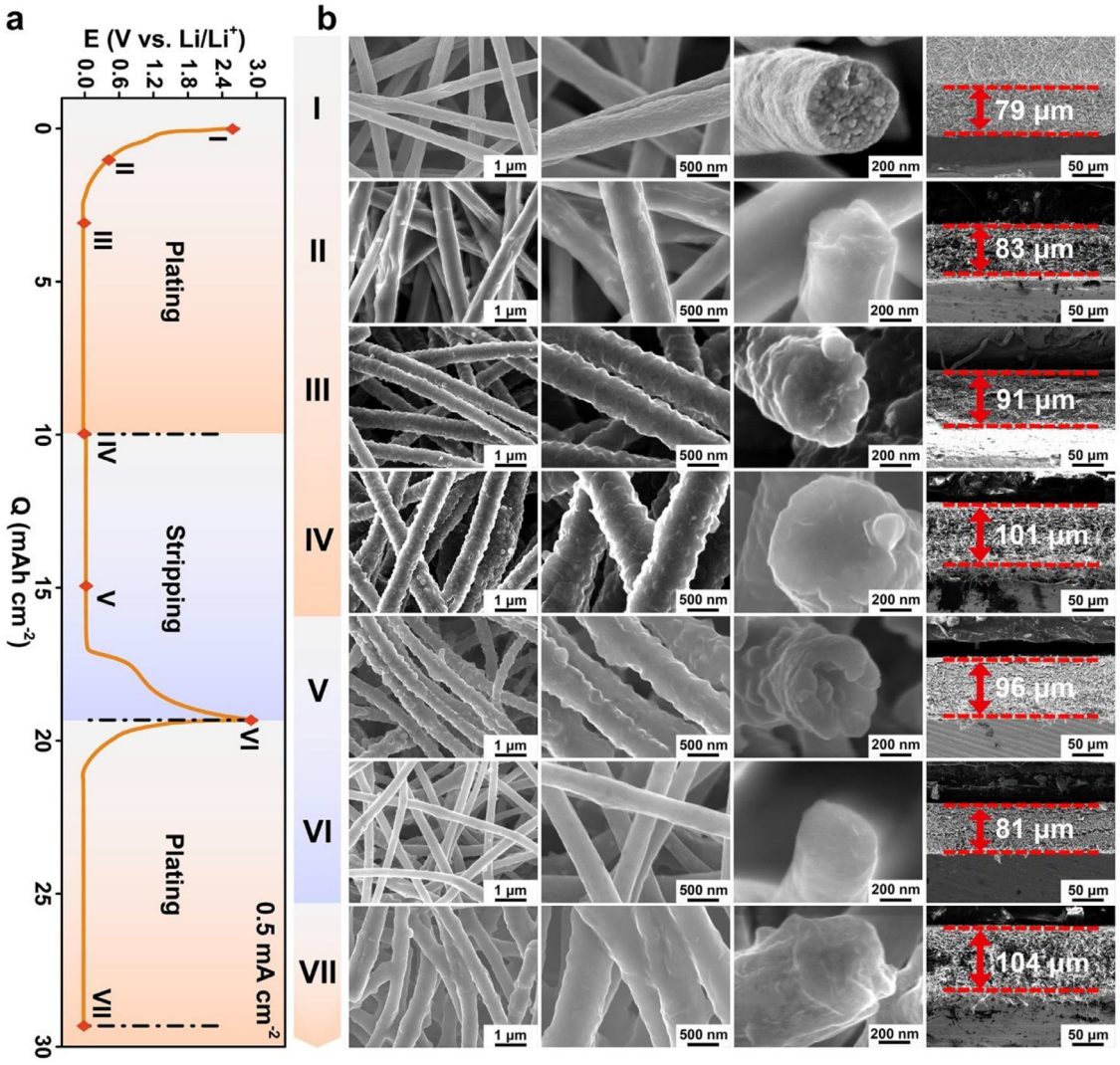


**Fig. 5.** (a) The plating/stripping curves of CoP@CNF for plating 10 mAh $cm^{-2}$ (20 h) of Li and stripping to 3 V at 0.5 mA $cm^{-2}$ on the 1st and 2nd cycles. (b) The corresponding SEM images of CoP@CNF at different Li plating/stripping states.

II), indicating that Li tends to nucleate homogeneously on individual fibers. It also suggests a good Li affinity of CoP, because the lithiation reaction of CoP dominates at this stage. As the capacity increases to the 3 mAh $cm^{-2}$ (6 h) that corresponds to the electrodepositing process of Li, spherical Li deposits uniformly cover the nanofibers (Fig. 5b III). The Li tends to evenly deposit onto the individual fibers during the continuous plating process (Fig. 5b IV). The thickness of the CoP@CNF electrode increases from 91 to 101 $\mu$m upon the Li plating process. No bulk Li is formed on the surface of electrode, revealing that the 3D host is effective to store Li and accommodate the volumetric expansion during Li deposition. In the subsequent stripping process, the fibrous CoP@CNF is continuously regulated with a decreasing diameter (Fig. 5b V). No residual Li deposits are observed on CoP@CNF after the full stripping of Li (Fig. 5b VI). The thickness of the film recovers to 81 $\mu$m, which is close to that of the pristine film (79 $\mu$m). The CE of initial cycle is 93.3%, thereby the increased 2 $\mu$m thickness is reasonable within consideration of the poorly reversible reaction of Li with N-doped carbon framework. In the second cycle of Li plating (Fig. 5b VII), the dendrite-free morphology is retained with Li depositing conformally over the fibers. By plating of 10 mAh $cm^{-2}$ of Li, the volume expansion is ca. 28% from state VI (81 $\mu$m) to VII (104 $\mu$m) of the 2nd cycle, which is the same as that from state I (79 $\mu$m) to IV (101 $\mu$m) of the 1st cycle. The CE is 98.2% of the 2nd cycle, 98.8% of the 5th cycle (Fig. S13a). The SEM images of the electrode after repeated cycling further verify the mechanical integrity of CoP@CNF framework (Fig. S13b). These results demonstrate that the CoP@CNF is capable of maintaining uniform Li deposition and suppressing dendrite evolution upon continuous cycling. However, massive Li bulks are formed on the CNF nanofibers upon prolonged plating and stripping, causing the growth of Li dendrites (Fig. S14). The absence of dendrites on CoP@CNF results from the doping of CoP with good Li affinity. The lithiophilic mixed ion/electron conductive skeleton provides well distributed Li nucleation sites and unobstructed mass transfer channels for electrolyte fluxion.

### 3.4. The performance of the cell with a $LiFePO_4$ cathode

To investigate the feasible application of the CoP@CNF@Li composite anode, the cell performance with a $LiFePO_4$ (LFP) cathode was evaluated. As shown in Fig. S15, the cell shows well overlapped galvanostatic voltage profiles with a plateau at 3.45 V (vs. $Li/Li^+$) and an initial capacity of 162 mAh $g^{-1}$ at 0.2 C (1 C = 170 mA $g^{-1}$). Charge–discharge profiles under different current densities show that the cell with CoP@CNF@Li exhibiting polarization values of 0.051, 0.141 and 0.392 V at 0.2, 2 and 10 C, respectively (Fig. 6a). In contrast, increased voltage polarization and capacity fading were observed for CNF@Li and Li foil. The respective polarization values are 0.058, 0.164 and 0.474 V for CNF@Li (Fig. 6b) and 0.071, 0.186 and 0.526 V for Li foil at 0.2, 2 and 10 C, respectively (Fig. 6c). Notably, a better rate capability is

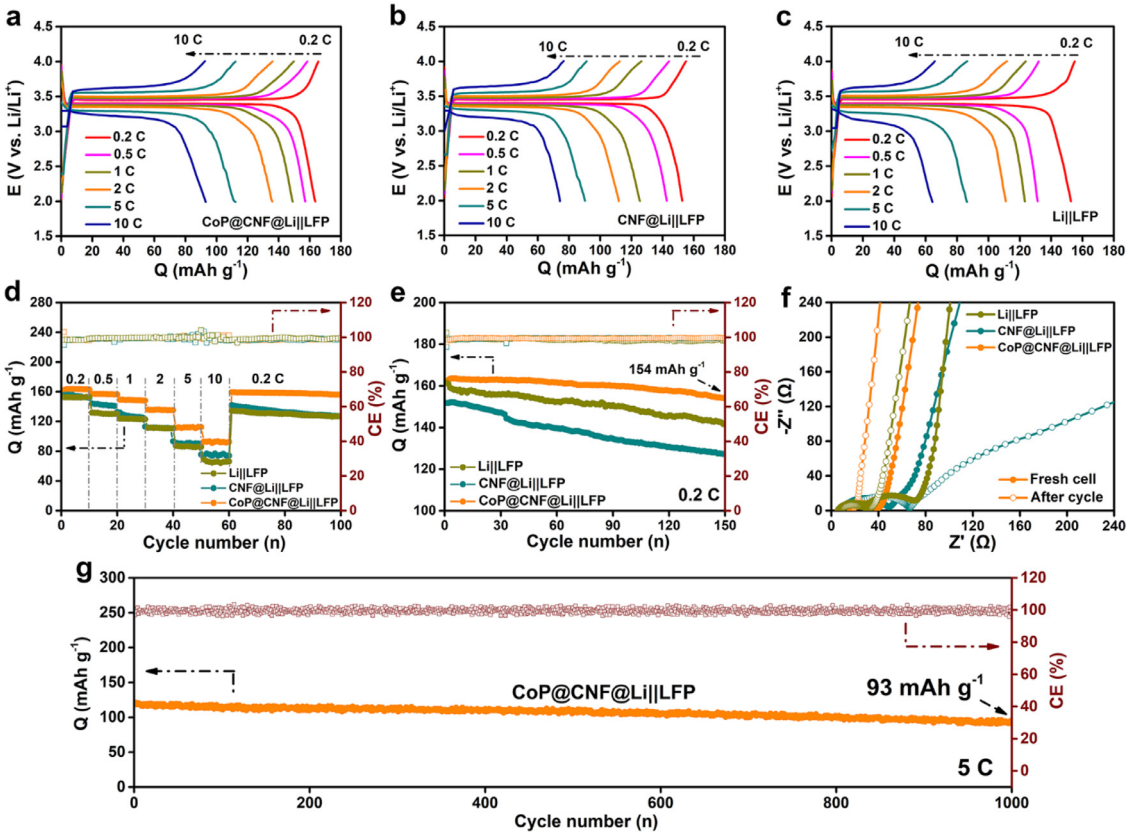


**Fig. 6.** (a–c) Voltage–capacity profiles of CoP@CNF@Li||LFP, CNF@Li||LFP and Li||LFP cells at 0.2 to 10 C (1 C = 170 mA $g^{-1}$), and (d) the corresponding rate performance. (e) The cyclic performance at 0.2 C. (f) EIS profiles of different anodes before and after cycling. (g) Long-term cycling of CoP@CNF@Li||LFP cell at 5 C.

achieved for CoP@CNF@Li||LFP (Fig. 6d). When reset from 10 to 0.2 C, a capacity of 161 mAh $g^{-1}$ is recovered. The specific capacity of 154 mAh $g^{-1}$ with a CE of 99.6% after 150 cycles is maintained for the cell with CoP@CNF@Li, compared with that of 98.6% and 99.3% with a Li or CNF@Li anode, respectively (Fig. 6e). These results convincingly confirm a uniformized ion/electron transport and stable Li deposition behavior in the CoP@CNF. EIS plots of these cells at different cycle states in detail were employed to determine the interfacial transport resistance (Fig. 6f and S16). CoP@CNF@Li exhibits the smallest $R_i$ of 39 (before cycling) and 17 Ω (after cycling), compared with 48 and 66 Ω for CNF@Li, and 71 and 32 Ω for Li, respectively. Impressively, the CoP@CNF@Li maintains 93 mAh $g^{-1}$ upon 1000 cycles along with an average CE of 99.2% at a high current density of 5 C (Fig. 6g). SEM images further verify the dendrite-free characteristic and integrity of CoP@CNF@Li after the long-term high-rate cycling (Fig. S17).

## 4. Conclusion

In summary, this work demonstrates the feasibility of a long-lifespan Li-metal anode enabled by a mixed ion/electron CoP@CNF skeleton reservoir. The chemical calculation suggests that the $Li^+$ is more readily adsorbed on the crystal surface of CoP, leading to a lower migration and nucleation barrier. The well-distributed lithiophilic CoP provides sufficient Li nucleation sites, and the conversion reaction between Li and CoP affords fast charge transport to tailor the uniform Li electrodeposition. Therefore, low overpotential and extended cyclic life of the symmetric CoP@CNF@Li cells are achieved. Furthermore, with a high-loading LFP cathode (1.5 mAh $cm^{-2}$), the CoP@CNF@Li||LFP cells exhibit good cyclic and rate performance. The rational design of CoP enhanced conductive matrix is a promising strategy for dendrite-free Li-metal batteries.

Li migration, nucleation and growth behavior regulated by a lithiophilic cobalt phosphide-doped carbon nanofibers derived ion/electron conductive framework

## Notes

The authors declare no competing financial interest.

## Supporting information

The Supporting Information is available free of charge on the Elsevier Publications website.

## Declaration of Competing Interest

The authors declare that they have no known competing financial interests or personal relationships that could have appeared to influence the work reported in this paper.

## CRediT authorship contribution statement

**Cuimei Fu:** Conceptualization, Data curation, Investigation, Formal analysis, Visualization, Writing – original draft, Writing – review & editing. **Shiru Lin:** Data curation, Software, Writing – original draft, Writing – review & editing. **Chengcheng Zhao:** Formal analysis, Investigation. **Jin Wang:** Visualization, Formal analysis. **Lina Wang:** Resources, Conceptualization, Funding acquisition, Project administration, Methodology, Supervision, Writing – review & editing. **Junwei Lucas Bao:** Funding acquisition, Project administration, Methodology, Supervision, Writing – review & editing. **Yonggang Wang:** Funding acquisition, Project administration. **Tianxi Liu:** Funding acquisition, Supervision, Project administration.

## Acknowledgments

Y. W. acknowledges financial support from the National Key Research and Development Program of China (2018YFE0201702). L. W. acknowledges financial support from the National Natural Science Foundation of China (21603030) and the State Key Laboratory for Modification of Chemical Fibers and Polymer Materials, Donghua University. J. L. B. acknowledges the start-up funding provided by Boston College and the Boston College Linux cluster for computational resources. L. W. acknowledges Prof. Yu Zhao at Soochow University for the helpful discussions. We also thank Elizabeth Donahue at Boston College for her editing help.

## Supplementary materials

Supplementary material associated with this article can be found, in the online version, at doi:10.1016/j.ensm.2021.11.009.

## References

[1] Y. Tian, G. Zeng, A. Rutt, T. Shi, H. Kim, J. Wang, J. Koettgen, Y. Sun, B. Ouyang, T. Chen, Z. Lun, Z. Rong, K. Persson, G. Ceder, Promises and challenges of next-generation "beyond Li-ion" batteries for electric vehicles and grid decarbonization, Chem. Rev. 121 (2021) 1623–1669, doi:10.1021/acs.chemrev.0c00767.

[2] J.B. Goodenough, K.S. Park, The Li-ion rechargeable battery: a perspective, J. Am. Chem. Soc. 135 (2013) 1167–1176, doi:10.1021/ja3091438.

[3] G. Xu, L. Huang, C. Lu, X. Zhou, G. Cui, Revealing the multilevel thermal safety of lithium batteries, Energy Storage Mater. 31 (2020) 72–86, doi:10.1016/j.ensm.2020.06.004.

[4] D. Lin, Y. Liu, Y. Cui, Reviving the lithium metal anode for high-energy batteries, Nat. Nanotechnol. 12 (2017) 194–206, doi:10.1038/nnano.2017.16.

[5] W. Cai, Y.X. Yao, G.L. Zhu, C. Yan, L.L. Jiang, C. He, J.Q. Huang, Q. Zhang, A review on energy chemistry of fast-charging anodes, Chem. Soc. Rev. 49 (2020) 3806–3833, doi:10.1039/C9CS00728H.

[6] X.B. Cheng, R. Zhang, C.Z. Zhao, Q. Zhang, Toward safe lithium metal anode in rechargeable batteries: a review, Chem. Rev. 117 (2017) 10403–10473, doi:10.1021/acs.chemrev.7b00115.

[7] X. Zhang, A. Wang, X. Liu, J. Luo, Dendrites in lithium metal anodes: suppression, regulation, and elimination, Acc. Chem. Res 52 (2019) 3223–3232, doi:10.1021/acs.accounts.9b00437.

[8] Y. Zhang, T.T. Zuo, J. Popovic, K. Lim, Y.X. Yin, J. Maier, Y.G. Guo, Towards better Li metal anodes: challenges and strategies, Mater. Today 33 (2020) 56–74, doi:10.1016/j.mattod.2019.09.018.

[9] F. Wu, Y.X. Yuan, X.B. Cheng, Y. Bai, Y. Li, C. Wu, Q. Zhang, Perspectives for restraining harsh lithium dendrite growth: towards robust lithium metal anodes, Energy Storage Mater. 15 (2018) 148–170, doi:10.1016/j.ensm.2018.03.024.

[10] M. Baloch, D. Shanmukaraj, O. Bondarchuk, E. Bekaert, T. Rojo, M. Armand, Variations on $Li_3N$ protective coating using *ex-situ* and *in-situ* techniques for Li in sulphur batteries, Energy Storage Mater. 9 (2017) 141–149, doi:10.1016/j.ensm.2017.06.016.

[11] Y. Luo, T. Li, H. Zhang, W. Liu, X. Zhang, J. Yan, H. Zhang, X. Li, Endogenous symbiotic $Li_3N$/cellulose skin to extend the cycle life of lithium anode, Angew. Chem. Int. Ed. 60 (2021) 11718–11724, doi:10.1002/anie.202017281.

[12] L. Wang, S. Fu, T. Zhao, J. Qian, N. Chen, L. Li, F. Wu, R. Chen, *In situ* formation of a LiF and Li–Al alloy anode protected layer on a Li metal anode with enhanced cycle life, J. Mater. Chem. A 8 (2020) 1247–1253, doi:10.1039/C9TA10965J.

[13] L. Chen, X. Fan, X. Ji, J. Chen, S. Hou, C. Wang, High-energy Li metal battery with lithiated host, Joule 3 (2019) 732–744, doi:10.1016/j.joule.2018.11.025.

[14] D. Kang, N. Hart, J. Koh, L. Ma, W. Liang, J. Xu, S. Sardar, J.P. Lemmon, Rearrange SEI with artificial organic layer for stable lithium metal anode, Energy Storage Mater. 24 (2020) 618–625, doi:10.1016/j.ensm.2019.06.014.

[15] C. Wu, H. Huang, W. Lu, Z. Wei, X. Ni, F. Sun, P. Qing, Z. Liu, J. Ma, W. Wei, L. Chen, C. Yan, L. Mai, Mg doped Li–LiB alloy with *in situ* formed lithiophilic LiB skeleton for lithium metal batteries, Adv. Sci. 7 (2020) 1902643, doi:10.1002/advs.201902643.

[16] H. Qiu, T. Tang, M. Asif, W. Li, T. Zhang, Y. Hou, Stable lithium metal anode enabled by lithium metal partial alloying, Nano Energy 65 (2019) 103989, doi:10.1016/j.nanoen.2019.103989.

[17] G. Yang, Y. Song, Q. Wang, L. Zhang, L. Deng, Review of ionic liquids containing, polymer/inorganic hybrid electrolytes for lithium metal batteries, Mater. Design. 190 (2020) 108563, doi:10.1016/j.matdes.2020.108563.

[18] P. Jankowski, W. Wieczorek, P. Johansson, Functional ionic liquids: cationic SEI-formers for lithium batteries, Energy Storage Mater. 20 (2019) 108–117, doi:10.1016/j.ensm.2019.04.024.

[19] T. Hou, G. Yang, N.N. Rajput, J. Self, S.-.W. Park, J. Nanda, K.A. Persson, The influence of FEC on the solvation structure and reduction reaction of $LiPF_6$/EC electrolytes and its implication for solid electrolyte interphase formation, Nano Energy 64 (2019) 103881, doi:10.1016/j.nanoen.2019.103881.

[20] A.B. Gunnarsdóttir, S. Vema, S. Menkin, L.E. Marbella, C.P. Grey, Investigating the effect of a fluoroethylene carbonate additive on lithium deposition and the solid electrolyte interphase in lithium metal batteries using *in situ* NMR spectroscopy, J. Mater. Chem. A 8 (2020) 14975–14992, doi:10.1039/D0TA05652A.

[21] S. Liu, X. Ji, N. Piao, J. Chen, N. Eidson, J. Xu, P. Wang, L. Chen, J. Zhang, T. Deng, S. Hou, T. Jin, H. Wan, J. Li, J. Tu, C. Wang, An inorganic-rich solid electrolyte interphase for advanced lithium-metal batteries in carbonate electrolytes, Angew. Chem. Int. Ed. 60 (2021) 3661–3671, doi:10.1002/anie.202012005.

[22] Z.L. Brown, S. Heiskanen, B.L. Lucht, Using triethyl phosphate to increase the solubility of $LiNO_3$ in carbonate electrolytes for improving the performance of the lithium metal anode, J. Electrochem. Soc. 166 (2019) A2523–A2527, doi:10.1149/2.0991912jes.

[23] C. Zhang, Q. Lan, Y. Liu, J. Wu, H. Shao, H. Zhan, Y. Yang, A dual-layered artificial solid electrolyte interphase formed by controlled electrochemical reduction of LiTFSI/DME-$LiNO_3$ for dendrite-free lithium metal anode, Electrochim. Acta 306 (2019) 407–419, doi:10.1016/j.electacta.2019.03.162.

[24] S. Jurng, Z.L. Brown, J. Kim, B.L. Lucht, Effect of electrolyte on the nanostructure of the solid electrolyte interphase (SEI) and performance of lithium metal anodes, Energy Environ. Sci. 11 (2018) 2600–2608, doi:10.1039/C8EE00364E.

[25] K. Qin, K. Holguin, M. Mohammadiroudbari, J. Huang, E.Y.S. Kim, R. Hall, C. Luo, Strategies in structure and electrolyte design for high-performance lithium metal batteries, Adv. Funct. Mater. 31 (2021) 2009694, doi:10.1002/adfm.202009694.

[26] R. Pathak, K. Chen, F. Wu, A.U. Mane, R.V. Bugga, J.W. Elam, Q. Qiao, Y. Zhou, Advanced strategies for the development of porous carbon as a Li host/current collector for lithium metal batteries, Energy Storage Mater. 41 (2021) 448–465, doi:10.1016/j.ensm.2021.06.015.

[27] X.Y. Yue, W.W. Wang, Q.C. Wang, J.K. Meng, X.X. Wang, Y. Song, Z.W. Fu, X.J. Wu, Y.N. Zhou, Cuprite-coated Cu foam skeleton host enabling lateral growth of lithium dendrites for advanced Li metal batteries, Energy Storage Mater. 21 (2019) 180–189, doi:10.1016/j.ensm.2018.12.007.

[28] Z. Zhang, J. Wang, X. Yan, S. Zhang, W. Yang, Z. Zhuang, W.Q. Han, *In-situ* growth of hierarchical N-doped CNTs/Ni Foam scaffold for dendrite-free lithium metal anode, Energy Storage Mater. 29 (2020) 332–340, doi:10.1016/j.ensm.2020.04.022.

[29] K. Yan, Z. Lu, H.W. Lee, F. Xiong, P.C. Hsu, Y. Li, J. Zhao, S. Chu, Y. Cui, Selective deposition and stable encapsulation of lithium through heterogeneous seeded growth, Nat. Energy 1 (2016) 16010, doi:10.1038/nenergy.2016.10.

[30] W. Guo, S. Liu, X. Guan, X. Zhang, X. Liu, J. Luo, Mixed ion and electron-conducting scaffolds for high-Rate lithium metal anodes, Adv. Energy Mater. 9 (2019) 1900193, doi:10.1002/aenm.201900193.

[31] C. Zhang, S. Liu, G. Li, C. Zhang, X. Liu, J. Luo, Incorporating ionic paths into 3D conducting scaffolds for high volumetric and areal capacity, high rate lithium-metal anodes, Adv. Mater 30 (2018) 1801328, doi:10.1002/adma.201801328.

[32] S.H. Kim, N.Y. Kim, U.J. Choe, J.M. Kim, Y.G. Lee, S.Y. Lee, Ultrahigh-energy-density flexible lithium-metal full cells based on conductive fibrous skeletons, Adv. Energy Mater. 11 (2021) 2100531, doi:10.1002/aenm.202100531.

[33] P. Zhai, Y. Wei, J. Xiao, W. Liu, J. Zuo, X. Gu, W. Yang, S. Cui, B. Li, S. Yang, Y. Gong, *In situ* generation of artificial solid-electrolyte interphases on 3D conducting scaffolds for high-performance lithium-metal anodes, Adv. Energy Mater. 10 (2020) 1903339, doi:10.1002/aenm.201903339.

[34] T.S. Wang, X. Liu, X. Zhao, P. He, C.W. Nan, L.Z. Fan, Regulating uniform Li plating/stripping via dual-conductive metal-organic frameworks for high-rate lithium metal batteries, Adv. Funct. Mater. 30 (2020) 2000786, doi:10.1002/adfm.202000786.

[35] H. Shi, M. Yue, C.J. Zhang, Y. Dong, P. Lu, S. Zheng, H. Huang, J. Chen, P. Wen, Z. Xu, Q. Zheng, X. Li, Y. Yu, Z.S. Wu, 3D flexible, conductive, and recyclable $Ti_3C_2T_x$ MXene-melamine foam for high-areal-capacity and long-lifetime alkali-metal anode, ACS Nano 14 (2020) 8678–8688, doi:10.1021/acsnano.0c03042.

[36] T. Zhang, H. Lu, J. Yang, Z. Xu, J. Wang, S.I. Hirano, Y. Guo, C. Liang, Stable lithium metal anode enabled by a lithiophilic and electron/ion conductive framework, ACS Nano 14 (2020) 5618–5627, doi:10.1021/acsnano.9b10083.

[37] Y. Han, Z. Sang, D. Liu, T. Zhang, J. Feng, W. Si, S.X. Dou, J. Liang, F. Hou, Lithiophilic and conductive $V_2O_3$/VN nanosheets as regulating layer for high-rate, high-areal capacity and dendrite-free lithium metal anodes, Chem. Eng. J. 420 (2021) 129787, doi:10.1016/j.cej.2021.129787.

[38] G. Kresse, J. Hafner, Ab initio molecular dynamics for liquid metals, Phys. Rev. B 47 (1993) 558–561, doi:10.1103/PhysRevB.47.558.

[39] P.E. Blöchl, Projector augmented-wave method, Phys. Rev. B 50 (1994) 17953–17979, doi:10.1103/PhysRevB.50.17953.

[40] J.P. Perdew, K. Burke, M. Ernzerhof, Generalized gradient approximation made simple, Phys. Rev. Lett. 77 (1996) 3865–3868, doi:10.1103/PhysRevLett.77.3865.

[41] E.R. Johnson, A.D. Becke, A post-Hartree-Fock model of intermolecular interactions: inclusion of higher-order corrections, J. Chem. Phys 124 (2006) 174104, doi:10.1063/1.2190220.

[42] S. Grimme, Semiempirical GGA-type density functional constructed with a long-range dispersion correction, J. Comput. Chem. 27 (2006) 1787–1799, doi:10.1002/jcc.20495.

[43] S. Grimme, J. Antony, S. Ehrlich, H. Krieg, A consistent and accurate ab initio parametrization of density functional dispersion correction (DFT-D) for the 94 elements H-Pu, J. Chem. Phys. 132 (2010) 154104, doi:10.1063/1.3382344.

[44] S. Grimme, S. Ehrlich, L. Goerigk, Effect of the damping function in dispersion corrected density functional theory, J. Comput. Chem. 32 (2011) 1456–1465, doi:10.1002/jcc.21759.

[45] H.J. Monkhorst, J.D. Pack, Special points for Brillouin-zone integrations, Phys. Rev. B 13 (1976) 5188–5192, doi:10.1103/PhysRevB.13.5188.

[46] G. Henkelman, B.P. Uberuaga, H. Jónsson, A climbing image nudged elastic band method for finding saddle points and minimum energy paths, J. Chem. Phys. 113 (2000) 9901–9904, doi:10.1063/1.1329672.

[47] L. Bengtsson, Dipole correction for surface supercell calculations, Phys. Rev. B 59 (1999) 12301–12304, doi:10.1103/PhysRevB.59.12301.

[48] K. Momma, F. Izumi, VESTA: a three-dimensional visualization system for electronic and structural analysis, J. Appl. Cryst. 41 (2008) 653–658, doi:10.1107/S0021889808012016.
[49] M. Chase Jr, C. Davies, J. Downey Jr, D. Frurip, R. McDonald, A. Syverud, NIST JANAF thermochemical Tables 1985 version 1.0. National Institute of Standards and Technology. Gaithersburg, MD, (1985) 20899. https://janaf.nist.gov/.
[50] V. Wang, N. Xu, J.C. Liu, G. Tang, W.T. Geng, VASPKIT: a user-friendly interface facilitating high-throughput computing and analysis using VASP code, Comput. Phys. Commun. 267 (2021) 108033, doi:10.1016/j.cpc.2021.108033.
[51] X. Yang, A.Y. Lu, Y. Zhu, M.N. Hedhili, S. Min, K.W. Huang, Y. Han, L.J. Li, CoP nanosheet assembly grown on carbon cloth: a highly efficient electrocatalyst for hydrogen generation, Nano Energy 15 (2015) 634–641, doi:10.1016/j.nanoen.2015.05.026.
[52] Y. Wang, P. Liang, H. Yang, W. Li, Z. Wang, Z. Liu, J. Wang, X. Shen, Hollow CoP nanoparticles embedded in two–dimensional N–doped carbon arrays enabling advanced Li–$SeS_2$ batteries with rapid kinetics, Mater. Today Energy 17 (2020) 100423, doi:10.1016/j.mtener.2020.100423.
[53] X.W. Wang, H.P. Guo, J. Liang, J.F. Zhang, B. Zhang, J.Z. Wang, W.B. Luo, H.K. Liu, S.X. Dou, An integrated free-standing flexible electrode with holey-structured 2D bimetallic phosphide nanosheets for sodium-ion batteries, Adv. Funct. Mater. 28 (2018) 1801016, doi:10.1002/adfm.201801016.
[54] Y.Y. Chen, Y. Zhang, W.J. Jiang, X. Zhang, Z. Dai, L.J. Wan, J.S. Hu, Pomegranate-like N,P-doped $Mo_2C$@C nanospheres as highly active electrocatalysts for alkaline hydrogen evolution, ACS Nano 10 (2016) 8851–8860, doi:10.1021/acsnano.6b04725.
[55] D. Li, S. Zhang, Q. Zhang, P. Kaghazchi, H. Qi, J. Liu, Z. Guo, L. Wang, Y. Wang, Pencil-drawing on nitrogen and sulfur co-doped carbon paper: an effective and stable host to pre-store Li for high-performance lithium–air batteries, Energy Storage Mater. 26 (2020) 593–603, doi:10.1016/j.ensm.2019.12.003.
[56] W. Du, F. Han, M. Zhang, C. Qian, X. Yang, Temperature-dependent synthesis of MOF-derived Co@N-doped carbon nanotube nanocomposites toward accelerated reduction of 4-nitrophenol, Compos. Commun. 25 (2021) 100718, doi:10.1016/j.coco.2021.100718.
[57] X. Cao, J. Deng, K. Pan, Electrospinning janus type CoOx/C nanofibers as electrocatalysts for oxygen reduction reaction, Adv. Fiber Mater. 2 (2020) 85–92.
[58] X. Huang, X. Xu, C. Li, D. Wu, D. Cheng, D. Cao, Vertical CoP nanoarray wrapped by N,P-doped carbon for hydrogen evolution reaction in both acidic and alkaline conditions, Adv. Energy Mater. 9 (2019) 1803970, doi:10.1002/aenm.201803970.
[59] X. Chen, X.R. Chen, T.Z. Hou, B.Q. Li, X.B. Cheng, R. Zhang, Q. Zhang, Lithiophilicity chemistry of heteroatom-doped carbon to guide uniform lithium nucleation in lithium metal anodes, Sci. Adv. 5 (2019) eaau7728, doi:10.1126/sciadv.aau7728.
[60] X. Wang, Y. Qian, L. Wang, H. Yang, H. Li, Y. Zhao, T. Liu, Sulfurized polyacrylonitrile cathodes with high compatibility in both ether and carbonate electrolytes for ultrastable lithium–sulfur batteries, Adv. Funct. Mater. 29 (2019) 1902929, doi:10.1002/adfm.201902929.
[61] G. Yang, X. Li, Z. Guan, Y. Tong, B. Xu, X. Wang, Z. Wang, L. Chen, Insights into Lithium and Sodium Storage in Porous Carbon, Nano Lett. 20 (2020) 3836–3843, doi:10.1021/acs.nanolett.0c00943.
[62] L.G. Bulusheva, A.V. Okotrub, A.G. Kurenya, H. Zhang, H. Zhang, X. Chen, H. Song, Electrochemical properties of nitrogen-doped carbon nanotube anode in Li-ion batteries, Carbon 49 (2011) 4013–4023 N Y, doi:10.1016/j.carbon.2011.05.043.
[63] P. Simon, Y. Gogotsi, B. Dunn, Where do batteries end and supercapacitors begin? Science 343 (2014) 1210–1211, doi:10.1126/science.1249625.
[64] J. Wang, J. Polleux, J. Lim, B. Dunn, Pseudocapacitive contributions to electrochemical energy storage in $TiO_2$ (Anatase) nanoparticles, J. Phys. Chem. C 111 (2007) 14925–14931, doi:10.1021/jp074464w.
[65] H. Buschmann, S. Berendts, B. Mogwitz, J. Janek, Lithium metal electrode kinetics and ionic conductivity of the solid lithium ion conductors "$Li_7La_3Zr_2O_{12}$" and $Li_{7-x}La_3Zr_{2-x}Ta_xO_{12}$ with garnet-type structure, J. Power Sources 206 (2012) 236–244, doi:10.1016/j.jpowsour.2012.01.094.
[66] R. Wang, J. Yu, J. Tang, R. Meng, L.F. Nazar, L. Huang, X. Liang, Insights into dendrite suppression by alloys and the fabrication of a flexible alloy-polymer protected lithium metal anode, Energy Storage Mater. 32 (2020) 178–184, doi:10.1016/j.ensm.2020.07.039.